In-plane magnetic-field-induced quantum anomalous Hall plateau transition

Jinlong Zhang,[1] Zhaochen Liu,[1] and Jing Wang ⊙[1,2,*]

[1]*State Key Laboratory of Surface Physics, Department of Physics, Fudan University, Shanghai 200433, China*
[2]*Institute for Nanoelectronic Devices and Quantum Computing, Fudan University, Shanghai 200433, China*

Axion insulator is a new state of quantum matter with a vanishing Chern number but a quantized topological axion response. We study the critical properties of the magnetic-field-induced quantum phase transition in axion insulators. Take the even septuple layer film $MnBi_2Te_4$ as a concrete example, We find the mirror symmetry breaking from in-plane magnetic field could induce an axion insulator to quantum anomalous Hall (QAH) insulator transition, which belongs to the generic integer quantum Hall plateau transition. The microscopic model proposed here explains the out-of-plane magnetic-field-induced QAH plateau transition observed in this system experimentally. The chiral Majorana fermion does not necessarily emerge at the QAH plateau transition in $MnBi_2Te_4$ due to strong exchange field, but may be quite feasible in its descendent materials $MnBi_4Te_7$ and $MnBi_6Te_{10}$.

I. INTRODUCTION

The magnetic topological insulators (TIs) [1] brings the opportunity to realize a large family of exotic topological phenomena [2–14]. One representative example is the quantum anomalous Hall (QAH) effect discovered in dilute magnetic TIs at low temperature [12]. Intrinsic magnetic TIs are ideal for realizing exotic quantum states and topological phase transitions at elevated temperatures. The recent theoretical prediction [15–17] and experimental realization of the first antiferromagnetic (AFM) TI [18] in $MnBi_2Te_4$ has attracted intensive interest in this new class of quantum materials [19–30]. The even septuple layer (SL) film is predicted to be the axion state with quantized topological magnetoelectric effect (TME) [15]. The axion state has been experimentally observed in 6 SL $MnBi_2Te_4$ with vanishing total Hall resistance ρ_{xy} (sum of top and bottom surface) and large longitudinal resistance ρ_{xx}, where an out-of-plane magnetic field could drive it into a state with $\rho_{xy} \rightarrow \pm h/e^2$ and $\rho_{xx} \rightarrow 0$ [24,25]. The plateau transition is of particular interest, which may provide a platform for chiral Majorana fermion mode (CMFM) based quantum computing by proximity coupling to the *s*-wave superconductor [8,31–33]. However, the large out-of-plane field will destroy the superconductivity. While the in-plane critical field of two-dimensional (2D) superconductors are found to be much larger than that of out-of-plane [34–36]. It is natural to ask whether in-plane field could induce a QAH plateau transition. If it does, what are the critical properties of the quantum phase transition? In addition, can it be used for realizing CMFM? In this paper, we address these issues by studying even SL $MnBi_2Te_4$ as a concrete example, which is generic for magnetic TIs.

The organization of this paper is as follows. Section II describes the effective model and phase diagram for the axion insulator in even SL $MnBi_2Te_4$. Section III presents a plateau transition induced by the in-plane magnetic field. Section IV presents the results on chiral topological superconductivity of this system in proximity to the *s*-wave superconductor. Section V presents a discussion on the experimental feasibility. Section VI concludes this paper. Some auxiliary materials are relegated to the Appendixes.

II. MODEL

A. Effective model

The (111) Dirac surface state of $MnBi_2Te_4$ is gapped due to time-reversal Θ breaking. The noncircular Fermi surface of surface states observed in angle-resolved photoemission spectroscopy (ARPES) [23] is from the-threefold warping term [37], where the surface model is $H(\vec{k}) = v(k_y\sigma_x - k_x\sigma_y) + (\lambda/2)(k_+^3 + k_-^3)\sigma_z + g_z\sigma_z$. Here v is the Dirac velocity, $k_\pm = k_x \pm ik_y$ with x axis along ΓK, λ is the warping parameter, σ_i are Pauli matrices acting on spin space, $g_z = J_z\langle S_z \rangle$ is the surface Zeeman term due to exchange field along the z axis introduced by surface ferromagnetic ordering, $\langle S_z \rangle$ is the mean-field expectation value of surface local spin along the z axis, $J_z < 0$ is the effective exchange parameter between the local moment and band electron. For simplicity, the particle-hole asymmetry is neglected. Defining the characteristic energy $\epsilon^* = v\sqrt{v/\lambda}$ and wave vector $\sqrt{v/\lambda}$, we plot in Fig. 1(a) a set of constant energy contours within the bulk gap, consistent with the first-principles calculations [15].

Now we turn to the zero Hall plateau state in even SL film. The low-energy physics is described by the massive Dirac surface states only, where the intrinsic Néel-type ordering introduces the opposite Zeeman term on two surfaces. The generic form of the effective Hamiltonian is

$$\mathcal{H}(\vec{k}) = v(k_y\sigma_x - k_x\sigma_y)\tau_z + \frac{\lambda}{2}(k_+^3 + k_-^3)\sigma_z\tau_z$$
$$+ g_z\sigma_z\tau_z + g_x\sigma_x + g_y\sigma_y, \quad (1)$$
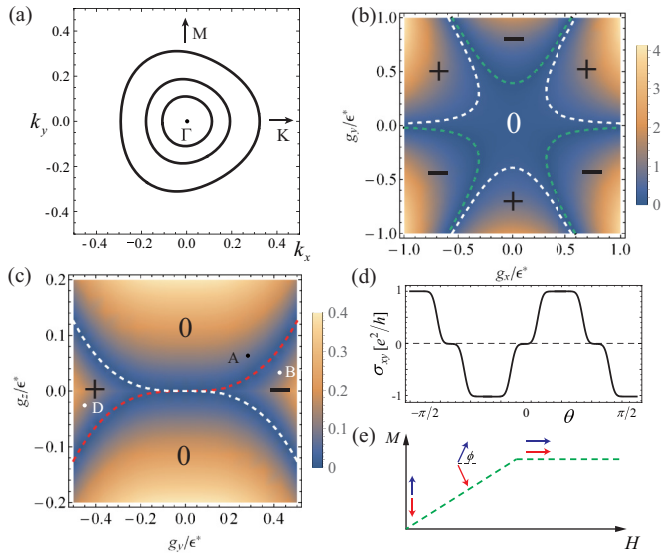
*wjingphys@fudan.edu.cn

FIG. 1. (a) Constant energy contour of $H(\vec{k})$. From inner to outer, the energy is $0.2\epsilon^*$, $0.25\epsilon^*$, $0.35\epsilon^*$. k_x and k_y are in unit of $\sqrt{v/\lambda}$. $\epsilon^* = 0.3$ eV, $g_z = 0.05$ eV [23]. (b) Phase diagram in (g_x, g_y) plane with $g_z/\epsilon^* = 0.06$. $\pm$ denotes $C = \pm 1$. (c) Phase diagram in (g_y, g_z) plane with $g_x = 0$. In both (b) and (c), the color bar represents the band gap in units of ϵ^*. (d) Sketch of Hall conductance versus the angle θ of in-plane magnetic field respect to x axis when $\mu = 0$. (e) Diagrammatic representation of AFM manipulation by in-plane magnetic field.

with the basis of $|t \uparrow\rangle$, $|t \downarrow\rangle$, $|b \uparrow\rangle$, and $|b \downarrow\rangle$, where t and b denote the top and bottom surface states and $\uparrow$ and $\downarrow$ represent spin up and down states, respectively. The Pauli matrices τ_i act on the layer. We neglect the hybridization between two surfaces, which is also negligible when the film exceeds 4 SL. $\vec{g}_\parallel \equiv (g_x, g_y) = J_\parallel(\langle S_x \rangle, \langle S_y \rangle)$ is an in-plane Zeeman-type exchange field, which can originate from the exchange field due to magnetization of Mn induced by the in-plane magnetic field, or the direct Zeeman coupling between the band electron and magnetic field. In the absence of field, the system is AFM with Néel order along the z axis. When the in-plane field is applied [Fig. 1(e)], the magnetic moments on two sublattices cant and a net magnetization gradually builds up proportional to the field as described by the Stoner-Wohlfarth model [38]. Interestingly, g_i ($i = x, y, z$) is continuously tunable. When $\lambda = \vec{g}_\parallel = 0$, the top and bottom surfaces have opposite half-quantized Hall conductance, and the system is a zero Hall plateau state with quantized topological axion response [11,15], which is also called an axion insulator [14]. Here we focus on $\lambda, \vec{g}_\parallel \neq 0$, which lead to an in-plane field-induced QAH plateau transition.

B. Phase diagram

A general symmetry analysis on the Hall conductance will help us to understand intuitively the in-plane field-induced QAH state. Θ breaking is necessary for nonzero σ_{xy}, which always exist in this system. In addition, when $\vec{g}_\parallel = 0$, the system has $\mathcal{I}\Theta$ symmetry, which constrains $\sigma_{xy} = 0$. Here $\mathcal{I}$ is the inversion operator. A finite $\vec{g}_\parallel$ leads to $\mathcal{I}\Theta$ breaking. Furthermore, the mirror symmetry in two dimensions also

leads to $\sigma_{xy} = 0$ [39,40]. With nonzero λ, the $MnBi_2Te_4$ film has only three mirror-symmetric ΓM directions if $g_z = 0$, thus, the pseudovector $\vec{g}_\parallel$ should not be perpendicular to ΓM (namely, not to parallel to ΓK) for nonzero σ_{xy}. If $\lambda = 0$, the system always has mirror symmetry perpendicular to $\vec{g}_\parallel$ with $\sigma_{xy} = 0$. Therefore, as g_i is continuously tuned by the in-plane field, the QAH plateau transition is expected.

The Hamiltonian in Eq. (1) is classified by the Chern number C. Since the topological invariants cannot change without closing the bulk gap, the phase diagram can be determined by first finding the phase boundaries as gapless regions in parameter spaces, and then calculate C of the gapped phases. The two surfaces in $\mathcal{H}(\vec{k})$ decouple with the band dispersion $E_{t/b} = \pm\sqrt{(g_z + \lambda(k_x^3 - 3k_x k_y^2))^2 + (g_y \mp v k_x)^2 + (g_x \pm v k_y)^2}$, with the gap closing point at $(k_x, k_y) = \pm(g_y/v, -g_x/v)$ and $g_z = -\lambda(k_x^3 - 3k_x k_y^2)$. This leads to the phase diagram shown in Fig. 1(c), which can be understood from the phase transition of the surface Dirac model. In Fig. 1(c), the white (red) line corresponds to the phase transition from top (bottom) surfaces. The gap of the top surface occurs at $(k_t^x, k_t^y) = (g_y/v, -g_x/v)$, where the effective model is rewritten as $H_t = m_t' \sigma_z + k_t^{y'} \sigma_x - k_t^{x'} \sigma_y$, with $k_t^{x'} = k_t^x - g_y/v$, $k_t^{y'} = k_t^y + g_x/v$ and $m_t' = g_z + (g_y^3 - 3g_x^2 g_y)/\epsilon^{*2}$. Such a continuous Dirac model has half-quantized Hall conductance due to the meron-type configuration in (k_x', k_y') space [2,41]. Namely

$$\sigma_{xy}^t \equiv C_t \frac{e^2}{h} = -\frac{\text{sgn}(m_t')}{2} \frac{e^2}{h}. \tag{2}$$

While for the bottom surface, $H_b = m_b' \sigma_z - k_b^{y'} \sigma_x + k_b^{x'} \sigma_y$ with $k_b^{x'} = k_b^x + g_y/v$, $k_b^{y'} = k_b^y - g_x/v$ and $m_b' = g_z - (g_y^3 - 3g_x^2 g_y)/\epsilon^{*2}$, thus $C_b = -\text{sgn}(m_b')/2$. Therefore, the total Chern number $C = C_t + C_b$. Furthermore, point A is adiabatically connected to $g_z \neq 0$ and the $\vec{g}_\parallel = 0$ limit with $C = 0$. While point B is adiabatically connected to $g_z = 0$ and $g_y \neq 0$ with $C = -1$ [40]. This can be understood by adding a small perturbation $g_z' \sigma_z$ into Eq. (1), and the system is further adiabatically connected to $g_z' < 0$ and $g_y = 0$, where $C = g_z'/|g_z'| = -1$ [42]. A similar analysis can be applied to point D. The Chern number of all gapped regimes is further determined from the C_{3z} rotational symmetry, as shown in Fig. 1(b).

III. PLATEAU TRANSITION

A. Domain

The above analysis on the Chern number of the surface Dirac model gives us a clear picture of the phase diagram in a uniform AFM system. However, AFM domains ($\uparrow\downarrow$ and $\downarrow\uparrow$) are probably constructed because they are degenerate energetically, as shown in Fig. 2.

The opposite AFM domains have opposite TME, thus even SL $MnBi_2Te_4$ has much reduced even the *vanishing* axion response due to multidomains. Fortunately, for the magnetoelectric crystals here, there are several ways to differentiate one AFM domain from the other. One simple way is to apply the electric field on $MnBi_2Te_4$, cooled below Néel temperature T_N without magnetic field, one can expect
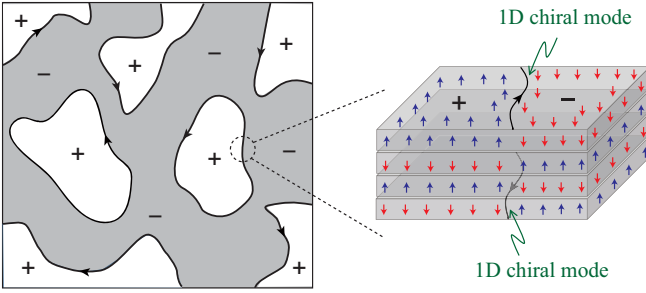
FIG. 2. AFM domains generically exist in even SL MnBi$_2$Te$_4$ film. There exist 1D chiral states (indicated by arrow lines) along AFM domain walls on t, b surfaces. On left panel only the top surface is shown. The symbols $+$ (white region) and $-$ (gray region) denote the upward ($\uparrow\downarrow\uparrow\downarrow$) and downward ($\downarrow\uparrow\downarrow\uparrow$) magnetic domains. The bottom surface is shown on right panel, where the chirality of 1D mode reverses.

FIG. 3. Sketch of in-plane magnetic field dependence of σ_{xy} and σ_{xx}.

that the directions of induced orbital magnetic moments are different from domain to domain. The AFM domain structure can be visualized by observing the polarity of the induced magnetic moment by Kerr technique. Another way is to use the second harmonic generation to measure Néel ordering [43]. There exist one-dimensional (1D) gapless chiral mode at AFM domain walls on both Dirac surface states as shown in Fig. 2, where the chiralities are opposite. This offers another way to differentiate the domains by imaging the conducting 1D chiral modes through scanning tunneling microscope or microwave impedance microscopy [44].

The intrinsic quantized TME in even SL MnBi$_2$Te$_4$ can be measured when the AFM domains are eliminated. In this case, the system is an axion insulator instead of a normal insulator. This can be achieved by the magnetoelectric field cooling with magnetic and electric fields applied simultaneously [45], which favors a distinct AFM single domain.

B. Plateau transition

From Eq. (2), by varying m_t' from some negative value to a positive value, we see a jump from $1/2$ to $-1/2$ in $\sigma_{xy}/(e^2/h)$. While the Dirac mass of the bottom surface does not change sign, this implies the Hall plateau transition from 0 to -1 in these units. Similarly, the bottom surface is responsible for the 1 to 0 transition when m_b' changes sign. They are non-degenerate as long as $g_z \neq 0$. By applying in-plane magnetic field, let us say along the ΓM direction, the QAH plateau transition happens at opposite fields with $m_t' = 0$ and $m_b' = 0$, respectively. The quenched disorder will generate spatially random perturbations to Eq. (1). There generically exist three types of randomness:

$$\mathcal{H}_g^j = g_z^j(x,y)\sigma_z + g_x^j(x,y)\sigma_x + g_y^j(x,y)\sigma_y,$$
$$\mathcal{H}_A^j = A_x^j(x,y)\sigma_y - A_y^j(x,y)\sigma_x, \qquad (3)$$
$$\mathcal{H}_V^j = V^j(x,y),$$

where $j = t, b$ simply means the two surfaces may feel different randomness. $\vec{A}^j \equiv (A_x^j, A_y^j)$, $\vec{g}^j \equiv (g_x^j, g_y^j, g_z^j)$, and V^j are nonuniform and random in space but constant in time. $\mathcal{H}_g$ corresponds to random exchange field induced by local spin
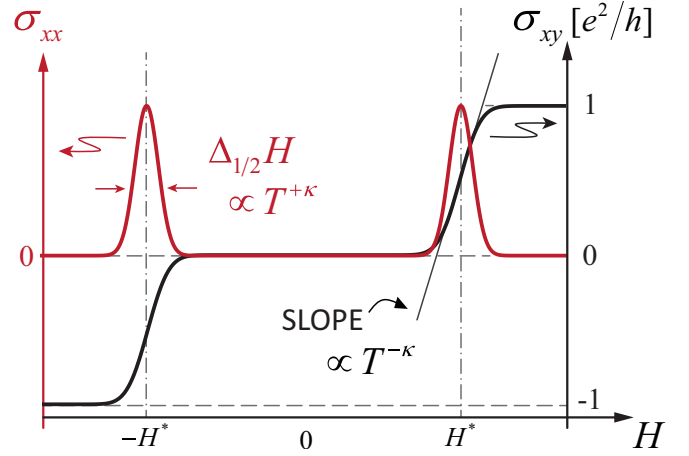
in magnetic domains. $\mathcal{H}_A$ is a random vector potential, which comes from the gauge coupling ($\vec{k} \rightarrow \vec{k} - \vec{A}$) with a random stray magnetic field in the system. $\mathcal{H}_V$ is the random scalar potential induced by impurities in the material. To be concrete, at $m_{t,b}' = 0$, we assume that all three random potentials are symmetrically distributed about zero mean. We also assume the interaction between the electrons can be neglected.

If the system has only a single AFM domain, then the in-plane field-induced QAH plateau transition here is exactly the *doubled* version of the random Dirac model for the integer QHE transition [46,47]. The fixed point of the random Dirac model is first conjectured to be a generic integer QHE fixed point [47–51], and later confirmed by exact mapping to the network model [52,53]. The mapping between the doubled Dirac model and network model has been studied in Ref. [42]. Therefore, the critical exponent obtained for the first [54] can be used for the second. The AFM multidomains introduce extra complications. There are three distinct cases. (i) $\uparrow$ and $\downarrow$ domains dominate on the top and bottom surfaces, respectively, then the QAH plateau transition is the same as in the single domain case. Namely, the in-plane field-induced $1/2$ to $-1/2$ transition on the top surface, while the bottom surface remains to be $-1/2$. (ii) $\uparrow$ domains dominate on both of two surfaces. The field induces $1/2$ to $-1/2$ transition on both surfaces. However, due to different random perturbations, the transitions on the two surfaces are generically nondegenerate. The system will experience discrete 1 to 0, then to -1 transition. (iii) $\uparrow$ and $\downarrow$ domains are the same, and the two surfaces are at a critical point. Then the system is no longer an insulator, but a critical metal with 1D *helical* modes percolating. In this state $\sigma_{xy} = 0$ due to averaged $\mathcal{I}\Theta$, but σ_{xx} is finite. A small in-plane field will drive the system into case (i). Therefore, AFM multidomains will not affect the critical behavior of in-plane field-induced QAH plateau transitions.

The critical phenomena in the above QAH plateau transition implies universal finite-size scaling behavior in the conductance and resistance matrices. More specifically, Fig. 3 shows the in-plane magnetic field dependence of σ_{xy} and σ_{xx}. There exist two critical points at $\pm H^*$ at which the localization length $\xi \propto |H - H^*|^{-\nu}$ diverges. The critical

exponent $\nu \approx 2.6$ [54,55], H^* is the critical external field of the plateau transition. The single parameter scaling [56] suggests the maximum slope in σ_{xy} diverges as a power law in temperature as $(\partial \sigma_{xy}/\partial H)_{\max} \propto T^{-\kappa}$. While the half-width of σ_{xx} peak vanishes like $\Delta_{1/2}H \propto T^\kappa$ [57]. Here $\kappa = p/2\nu$, and p is determined from the phase coherence length $L_{\rm in} \propto T^{-p/2}$ [58]. The statement for $\sigma_{\alpha\beta}$ can be directly translated into resistance $\rho_{\alpha\beta}$ through $\sigma_{\alpha\beta} = \rho_{\alpha\beta}/(\rho_{xx}^2 + \rho_{xy}^2)$. Still, one can observe two Hall resistance plateau transitions at $\pm H^*$, with $(\partial \rho_{xy}/\partial H)_{\max} \propto T^{-\kappa}$. However, ρ_{xx} will become a *single* peak due to an insulating state at zero Hall plateau, where around the critical field, $\rho_{xx} = f[(H - H^*)T^{-\kappa}]$ with f a regular function. Moreover, by rotating the in-plane field, $\sigma_{xy}/(e^2/h)$ will switch between 1, 0, -1, depending on the angle between in-plane field and crystalline orientation, and the above scaling behaviors also applies.

IV. CHIRAL TSC

The chiral topological superconductor (TSC) with odd $\mathcal{N}$ of CMFM was proposed to generically emerge at the QAH plateau transition in proximity to the s-wave superconductor [8]. This motivates us to study the phase diagram of the above system when proximity is coupled to the superconductor. The Bogoliubov–de Gennes (BdG) Hamiltonian is $H_{\rm BdG} = (1/2)\sum_{\vec{k}} \Psi_{\vec{k}}^\dagger \mathcal{H}_{\rm BdG} \Psi_{\vec{k}}$, with $\Psi_{\vec{k}} = (\psi_{\vec{k}}^T, \psi_{-\vec{k}}^\dagger)$, $\psi_{\vec{k}} = (c_{\vec{k}\uparrow}^t, c_{\vec{k}\downarrow}^t, c_{\vec{k}\uparrow}^b, c_{\vec{k}\downarrow}^b)$, and

$$\mathcal{H}_{\rm BdG}(\mathbf{k}) = \begin{pmatrix} \mathcal{H}(\vec{k}) - \mu & \Delta(\vec{k}) \\ \Delta^\dagger(\vec{k}) & -\mathcal{H}^*(-\vec{k}) + \mu \end{pmatrix},$$

$$\Delta(\vec{k}) = \begin{pmatrix} i\Delta_t \sigma_y & 0 \\ 0 & i\Delta_b \sigma_y \end{pmatrix}. \tag{4}$$

Here μ is the chemical potential, $\Delta_{t,b}$ are proximity-induced pairing gap functions on t and b surfaces, which are chosen as $\vec{k}$ independent due to the s-wave superconducting proximity effect. We consider low-temperature cases, and when the in-plane field $|\vec{H}|$ is smaller than the upper critical field of the parent superconductor, Δ_i remains finite and does not significantly change. The possible interlayer pairing is studied in Appendixes A and B.

The optimal condition for realizing the $\mathcal{N} = \pm 1$ TSC is to have inequivalent pairing on the two surfaces [31]. Thus here we only plot the phase diagram for $\mu = 0$ and $\Delta_b = 0$ in Fig. 4(a). One can see that only within the small circle around $\vec{g} = 0$ defined by $|\Delta_t| = \sum_i \sqrt{g_i^2} \equiv g$, the $\mathcal{N} = \pm 1$ TSC is realized. The phase boundary between $\mathcal{N} = 0$ and $\mathcal{N} = \pm 2$ in other regions is roughly the same as the boundary between $C = 0$ and $C = \pm 1$ in Fig. 1(c). This is simply because the in-plane field $\vec{g}_\parallel$ shifts the entire Fermi surface in the perpendicular direction in the Brillouin zone, and the energy between states at $\vec{k}$ and $-\vec{k}$ is no longer degenerate and leads to the pair-breaking effect from in-plane Zeeman field. When $g > |\Delta_t|$, the transitions are degenerate, namely directly from $\mathcal{N} = \pm 2$ to $\mathcal{N} = 0$ without intermediate phase. This is quite different from Ref. [31], where finite μ will enlarge $\mathcal{N} = \pm 1$ phases. Here finite μ will lead to a metallic state in bottom surface, and the top surface enters into a
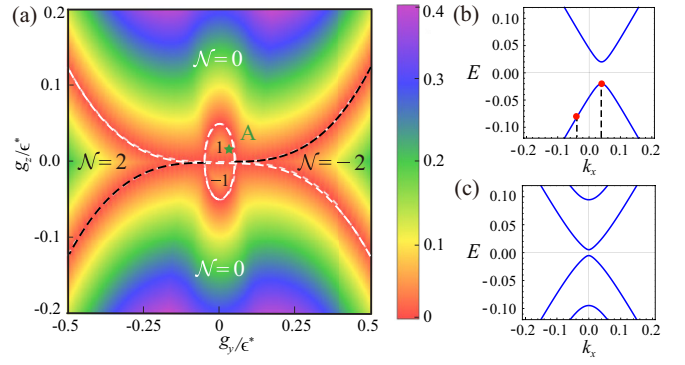

FIG. 4. (a) Phase diagram of even SL MnBi$_2$Te$_4$ superconductor hybrid system for $\mu = 0$, $\Delta_b = 0$, and $\Delta_t/\epsilon^* = 0.05$. The color represents the BdG gap. Here Δ_t is chosen to be unphysically large to see the small odd $\mathcal{N}$ TSC regions. (b) The single particle band structure of top surface for point A at $k_y = 0$ with $g_x = 0$, $g_y/\epsilon^* = 0.04$, $g_z/\epsilon^* = 0.02$, where the Zeeman energy difference between the states at $\vec{k}$ and $-\vec{k}$ is pair breaking for superconductivity. (c) The BdG spectrum of point A. The energy and k_x are in units of ϵ^* and $\sqrt{v/\lambda}$, respectively.

gapless superconductor with partial Bogoliubov Fermi surface [59] (see Appendix A). From the example studied above, we conclude that chiral TSC does not necessarily emerge at the QAH plateau transition if the exchange field is strong.

V. DISCUSSION

Finally we discuss the experimental feasibility. (i) Structure inversion asymmetry δV between the two surfaces should be smaller than $\max(m_t', m_b')$, then the field-induced QAH transition survives. (ii) We estimate $H_\parallel^*$ and the QAH gap, where the details are in Appendix D. Obviously, $H_\parallel^*$ depends on the field direction relative to the crystalline orientation from Fig. 1(b). Take ΓM for example, the transition is at $|g_z| = |g_y^3/\epsilon^{*2}|$. By assuming $J_z = J_\parallel$, then $\cos \phi^* = 0.95$ determines $H_\parallel^*$. ϕ is the angle between the magnetic moment and H. The in-plane magnetization $M_\parallel$ is linear in H, i.e., $S_{\rm sat} \cos \phi \propto H$, where $S_{\rm sat} \approx 3.6$ is the saturation magnetic moment [27]. Thus, $H_\parallel^* \approx 8.6$ T obtained when the in-plane moment roughly equals $S_{\rm sat} \cos \phi^*$ [17]. The estimated QAH gap is $2g_z^3/\epsilon^{*2} \approx 2.8$ meV ≈ 33 K. The large surface gap in MnBi$_2$Te$_4$ $g_z \approx 50$ meV [23] makes the in-plane QAH transition feasible in the experiment, which is impossible for dilute magnetic TIs. (iii) The above study can be directly applied to other magnetic TI systems such as MnBi$_4$Te$_7$ and MnBi$_6$Te$_{10}$ [28–30]. The AFM coupling and uniaxial anisotropy in these two materials are weaker compared to MnBi$_2$Te$_4$, which leads to a smaller critical $H_\parallel^*$. (iv) The out-of-plane field-induced QAH plateau transition found in Ref. [25] is similar to the case studied here, where AFM multidomains *spin-flop* and cant. The out-of-plane magnetic field dependence of the conductivity tensor is similar to that of in-plane field as in Fig. 3. At the spin-flop field, the system is described by Eq. (1) but with random $\vec{g}_\parallel$ and $g_z \approx 0$. By further increasing the field, $\vec{g}$ cants along the z-axis and induces 0 to ± 1 transition. The estimated critical field $H_\perp^* \approx 4.5$ T, which is consistent with the experimental value 4.58 T [25].

It is worth mentioning that the plateau transition in FM TIs always accompany the coercivity transition, where the abrupt coercivity transition may completely conceal the universal scaling of the QAH plateau transition [42]. Here there is no coercivity transition in $MnBi_2Te_4$ due to AFM ordering, which provides an ideal platform for studying critical behavior of the QAH plateau transition. (v) Lastly, $MnBi_2Te_4$ may not be suitable for chiral TSC due to strong exchange field. However, its descendent systems $MnBi_4Te_7$ and $MnBi_6Te_{10}$ thin films may be good platforms for the chiral Majorana fermion. There, one surface of Bi_2Te_3 is gapped by proximity coupled to the superconductor, and the other surface is magnetically gapped by $MnBi_2Te_4$.

VI. CONCLUSION

In summary, starting from the microscopic model for axion insulators, we study the critical properties of the in-plane magnetic-field-induced quantum phase transition from axion insulator to QAH insulator transition, which belongs to the generic integer QHE plateau transition. The microscopic model proposed here would explain the out-of-plane magnetic-field-induced QAH plateau transition observed in this system experimentally [25]. Without coercivity transition, the AFM axion insulator $MnBi_2Te_4$ provides an experimental platform to test the random Dirac model for QAH plateau transition. Furthermore, the CMFM does not necessarily emerge at the QAH plateau transition in $MnBi_2Te_4$ due to strong exchange field, but may be quite feasible in its descendent materials $MnBi_4Te_7$ and $MnBi_6Te_{10}$. We hope the theoretical work here can aid the study of the quantum phase transition and novel topological phases in axion insulators.

APPENDIX A: GAPLESS SUPERCONDUCTOR IN FINITE CHEMICAL POTENTIAL

For intralayer pairing as in Eq. (4) in the main text, in the presence of finite chemical potential, due to the pairing breaking effect from the in-plane exchange field, the gapped superconductor (SC) will become a gapless SC. Namely, the in-plane magnetic field will induce the gapped SC-gapless SC-normal state transition. Interestingly, in the gapless SC state, the system has partial Fermi surface (PFS) [59], where the spin texture and charge distribution are discussed.

The system is decoupled into top and bottom surface states. To start, the Hamiltonian for top surface is

$$H_{BdG}^t = \frac{1}{2} \sum_{\vec{k}} \phi_{\vec{k}}^\dagger \mathcal{H}_{BdG}^t \phi_{\vec{k}}, \quad (A1)$$
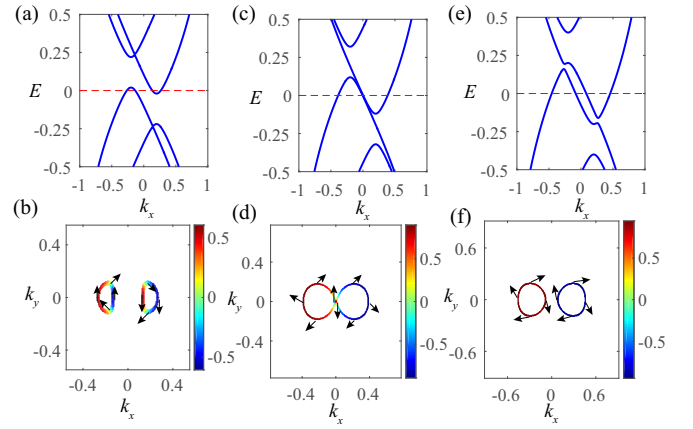

FIG. 5. The BdG spectra along k_x with $k_y = 0$ and Fermi surface with different g_y. (a, b) The energy spectra and PFS when $g_y = 0.12$. The colors denote the charge distribution in unit of e, and the arrow indicates the spin polarization in the $x - y$ plane. (c, d) $g_y = 0.22$. (e, f) $g_y = 0.3$. All other parameters are $g_x = g_z = 0$, $\Delta_t = 0.1$, $\mu = 0.2$.

where

$$\phi_{\vec{k}} = \left(c_{\vec{k}\uparrow}^t, c_{\vec{k}\downarrow}^t, c_{-\vec{k}\uparrow}^{t\dagger}, c_{-\vec{k}\downarrow}^{t\dagger} \right)^T \quad (A2)$$

and

$$\mathcal{H}_{BdG}^t(\mathbf{k}) = \begin{pmatrix} \mathcal{H}_t(\vec{k}) - \mu & i\Delta_t \sigma_y \\ -i\Delta_t \sigma_y & -\mathcal{H}_t^*(-\vec{k}) + \mu \end{pmatrix}, \quad (A3)$$

with $\mathcal{H}_t(\vec{k}) = k_y \sigma_x - k_x \sigma_y + (1/2)(k_+^3 + k_-^3)\sigma_z + g_z \sigma_z + g_y \sigma_y$. We define the charge $Q_{\vec{k}} \equiv -e\langle \vec{k}|c_{\vec{k}}^\dagger c_{\vec{k}} - h_{\vec{k}}^\dagger h_{\vec{k}}|\vec{k}\rangle$ and spin $\mathbf{S}_{\vec{k}} \equiv \langle \vec{k}|c_{\vec{k}}^\dagger \sigma c_{\vec{k}} - h_{\vec{k}}^\dagger \sigma^* h_{\vec{k}}|\vec{k}\rangle$, where $c_{\vec{k}} \equiv (c_{\vec{k}\uparrow}, c_{\vec{k}\downarrow})^T$, $h_{\vec{k}} \equiv (c_{-\vec{k}\uparrow}^\dagger, c_{-\vec{k}\downarrow}^\dagger)^T$ is the hole creation operator and $|\vec{k}\rangle$ is the wave function at $\vec{k}$. As shown in Figs. 5(a) and 5(b), with finite g_y, the Fermion surface is banana-shapes. The system is a gapless SC where parts of the normal state Fermi surface are gapped, while the ungapped parts are reconstructed into PFS of Bogliubov quasiparticle at zero energy. The two arcs have opposite charge and the same spin. With increasing g_y, the two PFS will involve into Figs. 5(d) and 5(f) without PFS.

The phase boundary of the two kinds of gapless SC [Figs. 5(b) and 5(f)] can be found by calculating the charge product $\mathcal{Q} \equiv \text{sgn}(Q_L)\text{sgn}(Q_R)$, where $Q_{L/R}$ is the charge on left and right sides on the same Fermion surface. Before the calculation, we discuss how the exchange field will affect the resulting SC state of the hybrid system. In the case of $g_\parallel = 0$ and finite g_z, the magnetic exchange field and the SC proximity coupling compete. When the SC gap wins, the system is a gapped chiral topological SC [31]. The chemical potential μ will enlarge the chiral topological SC phase. When the chemical potential is small and the warping effect is negligible, namely, no $\mathbf{k}^3$ terms. The system have the chiral symmetry $\mathcal{C} = \sigma_z \xi_y K$, $\mathcal{C}H(\mathbf{k})\mathcal{C}^{-1} = -H(\mathbf{k})$, so that the low-energy spectra is symmetrical about zero energy. With in-plane exchange field g_y, the chiral symmetry is broken, where the band minimum and maximum are not located on
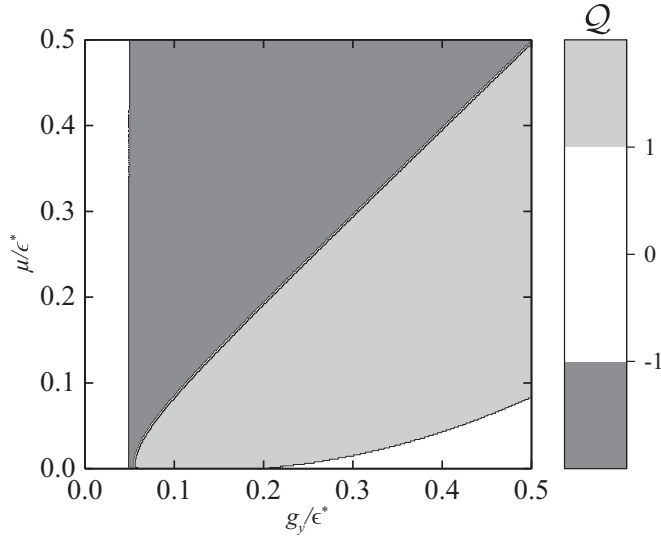
FIG. 6. The $g_y - \mu$ phase diagram with $\Delta_t = 0.05$, $g_x = 0$, $g_z = 0$. The white area is gapped SC. The gray area is gapless SC with PFS. The light gray area is gapless SC without PFS.

FIG. 8. Phase diagram of even SL MnBi$_2$Te$_4$ hybrid system with interlayer pairing for $g_x = 0$, $\mu = 0$, $\Delta_3 = 0.05$. The color represents the BdG gap. The white line is the phase boundary where the gap closes.

the same **k**, as shown in Fig. 5. The gapless SC will occur with g_y.

Figure 6 shows a $g_y - \mu$ phase diagram. There are three phases: gapped SC (white), gapless SC with PFS (gray), and gapless SC without PFS (light gray). For finite μ, by increasing the in-plane magnetic field, the system will experience "gapped SC-gapless SC with PFS-gapless SC without PFS," if the in-plane upper critical field is high enough. If the upper critical field is low, it will enter the normal state directly [59]. Meanwhile, the large μ will enlarge the phase area of gapless SC.

Finally, we consider the $g_y - g_z$ phase diagram with both top- and bottom-surfaces shown in Fig. 7. Figure 7(b) shows the normal state without SC in bottom surface. The white area is gapped, the other area is metal phased. In summary, we can find that the system will become chiral topological SC when SC gap > exchange gap > μ. The gapless SC is preferred with in-plane exchange field and large μ.

APPENDIX B: INTERLAYER PAIRING

When the film thickness is smaller than the phase coherence length of the parent s-wave SC, the interlayer pairing is possible. Here we only consider the zero-momentum pairing. The Hamiltonian is the Eq. (4) of the main text, where the pairing gap function is

$$\Delta(\vec{k}) = \begin{pmatrix} 0 & i\Delta_3\sigma_y \\ -i\Delta_3\sigma_y & 0 \end{pmatrix}. \tag{B1}$$

The phase diagram for this model is shown in Fig. 8. The band dispersion is $E = \pm\sqrt{\mathcal{E}_1 \pm \mathcal{E}_{2,\pm}}$. Thus the phase boundary is determined by $|\mathcal{E}|_1^2 = |\mathcal{E}_2|^2$. Here $\mathcal{E}_1 = g_z^{*2} + (g_y^* - k_x)^2 + k_y^2 + k_x^2(k_x^2 - 3k_y^2)^2 + \Delta_3^{*2}$ and $\mathcal{E}_{2,\pm} = 2\sqrt{g_z^{*2}k_x^2(k_x^2 - 3k_y^2)^2 + \Delta_3^{*2}[(g_y^* \pm k_x)^2 + k_y^2 + k_x^2(k_x^2 - 3k_y^2)^2]}$. $g^*, \Delta_3^*, \mathcal{E}_{1,2}$ are the dimensionless parameter in units of ϵ^*.

APPENDIX C: DOMAIN FORMATION

If Néel ordering starts at one point and develops to the whole crystal, there is no stray field and will be only one domain. Ordinarily, however, that is not the case. The crystalline imperfection is the common reason for AFM domain formation. Even in the perfect crystal, the lowering of free energy that accompanies an increase in entropy can lead to an equilibrium multidomain structure as shown in Fig. 2 of the main text. Such domains exist in MnBi$_2$Te$_4$, which is consistent with the recent ARPES measurement [60].

APPENDIX D: ESTIMATION OF H^*

Now we estimate the critical $H_\parallel^*$ when the QAH plateau transition happens. H^* depends on the field direction relative to the crystalline orientation. We take ΓM, for example: the phase boundary is determined by the sign change of $m'_{t,b}$,
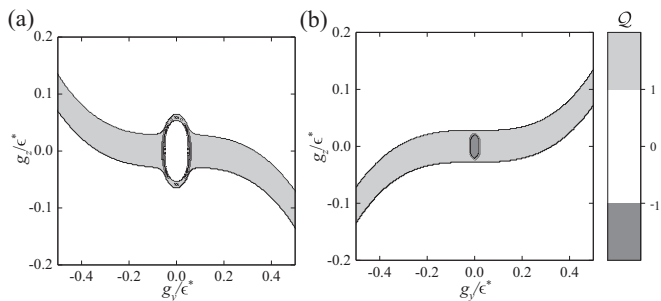

FIG. 7. (a, b) The $g_y - g_z$ phase diagram of top and bottom layer, respectively. With $\Delta_t = 0.05$, $g_x = 0$, $\mu = 0.02$. In (a), the white, gray, light gray area is gapped SC, gapless SC with PFS, gapless SC without PFS.
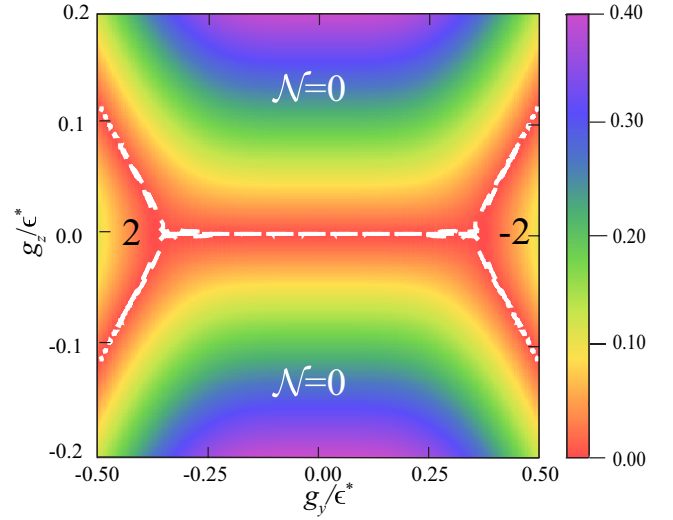
which is

$$|g_z| = |g_y^3/\epsilon^{*2}|. \tag{D1}$$

We have $g_z = J_z \langle S_z \rangle = J_z S_{\text{sat}} \langle s_z \rangle$ and $g_y = J_\| \langle S_y \rangle = J_\| S_{\text{sat}} \langle s_y \rangle$. This leads to

$$J_z S_{\text{sat}} \langle s_z \rangle = \frac{1}{\epsilon^{*2}} (J_\| S_{\text{sat}} \langle s_y \rangle)^3. \tag{D2}$$

Here S_{sat} is the saturation magnetic moment. Together with

$$\langle s_z \rangle^2 + \langle s_y \rangle^2 = (1/2)^2. \tag{D3}$$

From Eqs. (D2) and (D3), one can get the relation between $\langle s_z \rangle$ and $\langle s_y \rangle$, namely, the angle ϕ of spin direction relative to the y-axis, $\tan \phi = \langle s_z \rangle / \langle s_y \rangle$. For simplicity, we assume $J_z = J_\| = J$, therefore, we have

$$J S_{\text{sat}} \langle s_z \rangle = \frac{(J S_{\text{sat}})^3}{\epsilon^{*2}} \langle s_y \rangle^3. \tag{D4}$$

From the Dirac gap of (111) surface state of $MnBi_2Te_4$, we have $J(S_{\text{sat}}/2) = 2g_z \approx 0.15$ eV. $\epsilon^* \approx 0.3$ eV. Therefore, we have $\langle s_z \rangle \equiv \langle s_y \rangle^3$. So $\cos \phi^* = 0.95$ determines the critical H^*.

From the Stoner-Wohlfarth model, in the macrospin approximation, the energy density of one sublattice with uniaxial anisotropy K and subjected to an external magnetic field H is

$$E = J_A M_s^2 \cos(2\varphi) + K \cos^2(\varphi) - \mu_0 H M_s \cos(\varphi), \tag{D5}$$

where φ is the angle between **H** and the magnetic moment of the sublattice, J_A is the AFM exchange energy, M_s is the saturation magnetization of one sublattice. As shown in Fig. 1(e) in the main text, the in-plane magnetic field is applied, which is perpendicular to the easy axis. The magnetic moments of the two sublattices cant and a net magnetization **M** gradually builds up proportional to the field. This can be obtained by the minimization of E with respect to φ, namely,

$$\frac{\partial E}{\partial \varphi} = -2J_A M_s^2 \sin 2\varphi - 2K \cos \varphi \sin \varphi + \mu_0 H M_s \sin \varphi = 0. \tag{D6}$$

Therefore, the in-plane magnetization (or magnetic moment) is proportional to H,

$$M_\| \equiv M_s \cos \varphi = \frac{\mu_0 M_s^2}{4J_A M_s^2 + 2K} H \equiv \chi H. \tag{D7}$$

The χ is inverse proportional to K. Namely, the large uniaxial magnetic anisotropy will lead to smaller χ, then a larger H to make in-plane $M_\|$ to become saturate. This is consistent with the experiment in Ref. [17]. From the experiment, $S_{\text{sat}} \approx 3.6$ [27], and H^* is determined by $S_{\text{sat}} \cos \varphi^*$, which leads to $H_\|^* \approx 8.6$ T.

Furthermore, the above estimation of $H_\|^*$ could also apply to the out-of-plane field-induced QAH plateau transition. In fact, the in-plane magnetic-field-induced QAH plateau transition studied here directly applies to the out-of-plane field-induced QAH plateau transition found in Ref. [25]. With the out-of-plane field $H_\perp$, the AFM multidomains *spin-flop* and cant. This can be seen from Eq. (D5). Since K is small compared to J_A [15], the sublattice magnetization remains in the z-direction with zero net magnetization, until the magnetic field compensates the anisotropy. This is the spin-flop field which occurs at $\mu_0 H_{sf} \approx \sqrt{2KJ_A}$. After the spin-flop field, the sublattice magnetization cant increasingly in the direction of **H** and the net magnetization is linear proportional to **H**. Namely, $M_\perp = \chi'(H_\perp - H_{sf})$.

At the spin-flop field, the system is described by Eq. (1) of the main text but with random $\vec{g}_\|$ and $g_z \approx 0$. By further increasing the field, $\vec{g}$ cants along the z-axis and induces 0 to ± 1 transition. The critical field is again determined by Eq. (D1). Following the same procedure in the above, the estimated critical field $H_\perp^* \approx 4.5$ T, which is consistent with the experimental value 4.58 T [25], further validates our model.

Finally, we comment on the $MnBi_4Te_7$ and $MnBi_6Te_{10}$. In the thin film of the two systems, the in-plane field could also induce the QAH plateau transitions. Due to much larger separation between two Mn interlayers, both J_A and K is smaller compared to $MnBi_2Te_4$. This leads to much larger χ and smaller saturation field H_{sat}, which has been experimental verified in Refs. [29,30].

[1] Y. Tokura, K. Yasuda, and A. Tsukazaki, Nat. Rev. Phys. **1**, 126 (2019).

[2] X.-L. Qi, T. L. Hughes, and S.-C. Zhang, Phys. Rev. B **78**, 195424 (2008).

[3] M. Z. Hasan and C. L. Kane, Rev. Mod. Phys. **82**, 3045 (2010).

[4] X.-L. Qi and S.-C. Zhang, Rev. Mod. Phys. **83**, 1057 (2011).

[5] J. Wang and S.-C. Zhang, Nat. Mater. **16**, 1062 (2017).

[6] X.-L. Qi, R. Li, J. Zang, and S.-C. Zhang, Science **323**, 1184 (2009).

[7] R. Li, J. Wang, X. L. Qi, and S. C. Zhang, Nat. Phys. **6**, 284 (2010).

[8] X.-L. Qi, T. L. Hughes, and S.-C. Zhang, Phys. Rev. B **82**, 184516 (2010).

[9] R. Yu, W. Zhang, H.-J. Zhang, S.-C. Zhang, X. Dai, and Z. Fang, Science **329**, 61 (2010).

[10] K. Nomura and N. Nagaosa, Phys. Rev. Lett. **106**, 166802 (2011).

[11] J. Wang, B. Lian, X.-L. Qi, and S.-C. Zhang, Phys. Rev. B **92**, 081107(R) (2015).

[12] C.-Z. Chang, J. Zhang, X. Feng, J. Shen, Z. Zhang, M. Guo, K. Li, Y. Ou, P. Wei, L.-L. Wang, Z.-Q. Ji, Y. Feng, S. Ji, X. Chen, J. Jia, X. Dai, Z. Fang, S.-C. Zhang, K. He, Y. Wang, L. Lu, X.-C. Ma, and Q.-K. Xue, Science **340**, 167 (2013).

[13] J. Wang, B. Lian, and S.-C. Zhang, Phys. Scr. **T164**, 014003 (2015).

[14] M. Mogi, M. Kawamura, R. Yoshimi, A. Tsukazaki, Y. Kozuka, N. Shirakawa, K. S. Takahashi, M. Kawasaki, and Y. Tokura, Nat. Mater. **16**, 516 (2017).

[15] D. Zhang, M. Shi, T. Zhu, D. Xing, H. Zhang, and J. Wang, Phys. Rev. Lett. **122**, 206401 (2019).

[16] J. Li, Y. Li, S. Du, Z. Wang, B.-L. Gu, S.-C. Zhang, K. He, W. Duan, and Y. Xu, Sci. Adv. **5**, eaaw5685 (2019).

[17] M. M. Otrokov, I. I. Klimovskikh, H. Bentmann, A. Zeugner, Z. S. Aliev, S. Gass, A. U. B. Wolter, A. V. Koroleva, D. Estyunin, A. M. Shikin, M. Blanco-Rey, M. Hoffmann, A. Y. Vyazovskaya, S. V. Eremeev, Y. M. Koroteev, I. R. Amiraslanov, M. B. Babanly, N. T. Mamedov, N. A. Abdullayev, V. N. Zverev, B. Büchner, E. F. Schwier, S. Kumar, A. Kimura, L. Petaccia, G. Di Santo, R. C. Vidal, S. Schatz, K. Kißner, C.-H. Min, S. K. Moser, T. R. F. Peixoto, F. Reinert, A. Ernst, P. M. Echenique, A. Isaeva, and E. V. Chulkov, arXiv:1809.07389.

[18] R. S. K. Mong, A. M. Essin, and J. E. Moore, Phys. Rev. B **81**, 245209 (2010).

[19] Y. Gong, J. Guo, J. Li, K. Zhu, M. Liao, X. Liu, Q. Zhang, L. Gu, L. Tang, X. Feng, D. Zhang, W. Li, C. Song, L. Wang, P. Yu, X. Chen, Y. Wang, H. Yao, W. Duan, Y. Xu, S.-C. Zhang, X. Ma, Q.-K. Xue, and K. He, Chin. Phys. Lett. **36**, 076801 (2019).

[20] M. M. Otrokov, I. P. Rusinov, M. Blanco-Rey, M. Hoffmann, A. Y. Vyazovskaya, S. V. Eremeev, A. Ernst, P. M. Echenique, A. Arnau, and E. V. Chulkov, Phys. Rev. Lett. **122**, 107202 (2019).

[21] S. H. Lee, Y. Zhu, Y. Wang, L. Miao, T. Pillsbury, H. Yi, S. Kempinger, J. Hu, C. A. Heikes, P. Quarterman, W. Ratcliff, J. A. Borchers, H. Zhang, X. Ke, D. Graf, N. Alem, C.-Z. Chang, N. Samarth, and Z. Mao, Phys. Rev. Res. **1**, 012011(R) (2019).

[22] J.-Q. Yan, Q. Zhang, T. Heitmann, Z. Huang, K. Y. Chen, J.-G. Cheng, W. Wu, D. Vaknin, B. C. Sales, and R. J. McQueeney, Phys. Rev. Mater. **3**, 064202 (2019).

[23] R. C. Vidal, H. Bentmann, T. R. F. Peixoto, A. Zeugner, S. Moser, C.-H. Min, S. Schatz, K. Kißner, M. Ünzelmann, C. I. Fornari, H. B. Vasili, M. Valvidares, K. Sakamoto, D. Mondal, J. Fujii, I. Vobornik, S. Jung, C. Cacho, T. K. Kim, R. J. Koch, C. Jozwiak, A. Bostwick, J. D. Denlinger, E. Rotenberg, J. Buck, M. Hoesch, F. Diekmann, S. Rohlf, M. Kalläne, K. Rossnagel, M. M. Otrokov, E. V. Chulkov, M. Ruck, A. Isaeva, and F. Reinert, Phys. Rev. B **100**, 121104(R) (2019).

[24] Y. Deng, Y. Yu, M. Z. Shi, J. Wang, X. H. Chen, and Y. Zhang, arXiv:1904.11468.

[25] C. Liu, Y. Wang, H. Li, Y. Wu, Y. Li, J. Li, K. He, Y. Xu, J. Zhang, and Y. Wang, arXiv:1905.00715.

[26] B. Chen, F. Fei, D. Zhang, B. Zhang, W. Liu, S. Zhang, P. Wang, B. Wei, Y. Zhang, Z. Zuo, J. Guo, Q. Liu, Z. Wang, X. Wu, J. Zong, X. Xie, W. Chen, Z. Sun, S. Wang, Y. Zhang, M. Zhang, X. Wang, F. Song, H. Zhang, D. Shen, and B. Wang, Nat. Commun. **10**, 4469 (2019).

[27] J.-Q. Yan, S. Okamoto, M. A. McGuire, A. F. May, R. J. McQueeney, and B. C. Sales, Phys. Rev. B **100**, 104409 (2019).

[28] Z. S. Aliev, I. R. Amiraslanov, D. I. Nasonova, A. V. Shevelkov, N. A. Abdullayev, Z. A. Jahangirli, E. N. Orujlu, M. M. Otrokov, N. T. Mamedov, M. B. Babanly, and E. V. Chulkov, J. Alloys Compd. **789**, 443 (2019).

[29] C. Hu, X. Zhou, P. Liu, J. Liu, P. Hao, E. Emmanouilidou, H. Sun, Y. Liu, H. Brawer, A. P. Ramirez, H. Cao, Q. Liu, D. Dessau, and N. Ni, arXiv:1905.02154.

[30] J. Wu, F. Liu, M. Sasase, K. Ienaga, Y. Obata, R. Yukawa, K. Horiba, H. Kumigashira, S. Okuma, T. Inoshita, and H. Hosono, arXiv:1905.02385.

[31] J. Wang, Q. Zhou, B. Lian, and S.-C. Zhang, Phys. Rev. B **92**, 064520 (2015).

[32] B. Lian, J. Wang, X.-Q. Sun, A. Vaezi, and S.-C. Zhang, Phys. Rev. B **97**, 125408 (2018).

[33] B. Lian, X.-Q. Sun, A. Vaezi, X.-L. Qi, and S.-C. Zhang, Proc. Natl. Acad. Sci. USA **115**, 10938 (2018).

[34] C. P. Poole, Jr., H. A. Farach, R. J. Creswick, and R. Prozorov, *Superconductivity*, 3rd ed. (Elsevier, Amsterdam, 2014).

[35] J. M. Lu, O. Zheliuk, I. Leermakers, N. F. Q. Yuan, U. Zeitler, K. T. Law, and J. T. Ye, Science **350**, 1353 (2015).

[36] X. Xi, Z. Wang, W. Zhao, J.-H. Park, K. T. Law, H. Berger, L. Forró, J. Shan, and K. F. Mak, Nat. Phys. **12**, 139 (2016).

[37] L. Fu, Phys. Rev. Lett. **103**, 266801 (2009).

[38] V. Baltz, A. Manchon, M. Tsoi, T. Moriyama, T. Ono, and Y. Tserkovnyak, Rev. Mod. Phys. **90**, 015005 (2018).

[39] C. Fang, M. J. Gilbert, and B. A. Bernevig, Phys. Rev. B **86**, 115112 (2012).

[40] X. Liu, H.-C. Hsu, and C.-X. Liu, Phys. Rev. Lett. **111**, 086802 (2013).

[41] A. N. Redlich, Phys. Rev. D **29**, 2366 (1984).

[42] J. Wang, B. Lian, and S.-C. Zhang, Phys. Rev. B **89**, 085106 (2014).

[43] M. Fiebig, V. V. Pavlov, and R. V. Pisarev, J. Opt. Soc. Am. B **22**, 96 (2005).

[44] K. Lai, M. Nakamura, W. Kundhikanjana, M. Kawasaki, Y. Tokura, M. A. Kelly, and Z.-X. Shen, Science **329**, 190 (2010).

[45] P. Borisov, A. Hochstrat, X. Chen, W. Kleemann, and C. Binek, Phys. Rev. Lett. **94**, 117203 (2005).

[46] M. P. Fisher and E. Fradkin, Nucl. Phys. B **251**, 457 (1985).

[47] A. W. W. Ludwig, M. P. A. Fisher, R. Shankar, and G. Grinstein, Phys. Rev. B **50**, 7526 (1994).

[48] S. Kivelson, D.-H. Lee, and S.-C. Zhang, Phys. Rev. B **46**, 2223 (1992).

[49] B. Huckestein, Rev. Mod. Phys. **67**, 357 (1995).

[50] S. L. Sondhi, S. M. Girvin, J. P. Carini, and D. Shahar, Rev. Mod. Phys. **69**, 315 (1997).

[51] B. Kramer, T. Ohtsuki, and S. Kettemann, Phys. Rep. **417**, 211 (2005).

[52] J. T. Chalker and P. D. Coddington, J. Phys. C **21**, 2665 (1988).

[53] C.-M. Ho and J. T. Chalker, Phys. Rev. B **54**, 8708 (1996).

[54] K. Slevin and T. Ohtsuki, Phys. Rev. B **80**, 041304(R) (2009).

[55] W. Li, C. L. Vicente, J. S. Xia, W. Pan, D. C. Tsui, L. N. Pfeiffer, and K. W. West, Phys. Rev. Lett. **102**, 216801 (2009).

[56] A. M. M. Pruisken, Phys. Rev. Lett. **61**, 1297 (1988).

[57] D. G. Polyakov and B. I. Shklovskii, Phys. Rev. B **48**, 11167 (1993).

[58] D. J. Thouless, Phys. Rev. Lett. **39**, 1167 (1977).

[59] N. F. Q. Yuan and L. Fu, Phys. Rev. B **97**, 115139 (2018).

[60] Y. J. Chen, L. X. Xu, J. H. Li, Y. W. Li, C. F. Zhang, H. Li, Y. Wu, A. J. Liang, C. Chen, S. W. Jung, C. Cacho, H. Y. Wang, Y. H. Mao, S. Liu, M. X. Wang, Y. F. Guo, Y. Xu, Z. K. Liu, L. X. Yang, and Y. L. Chen, arXiv:1907.05119.